PAPER • OPEN ACCESS

Single GaAs nanowire based photodetector fabricated by dielectrophoresis

To cite this article: Carlos García Núñez *et al* 2020 *Nanotechnology* **31** 225604

View the article online for updates and enhancements.

Single GaAs nanowire based photodetector fabricated by dielectrophoresis

Carlos García Núñez[1,2] , Alejandro F Braña[1] , Nair López[1] ,
José L Pau[1] and Basilio J García[1]

[1] Electronics and Semiconductors Group (ELySE), Applied Physics Department, Universidad Autónoma de Madrid (UAM), 28049 Madrid, Spain
[2] Scottish Universities Physics Alliance (SUPA), Institute of Thin Films, Sensors & Imaging (TFSI), University of the West of Scotland (UWS), Paisley PA1 2BE, United Kingdom

E-mail: carlos.garcianunez@uws.ac.uk

CrossMark

Abstract

Mechanical manipulation of nanowires (NWs) for their integration in electronics is still problematic because of their reduced dimensions, risking to produce mechanical damage to the NW structure and electronic properties during the assembly process. In this regard, contactless NW manipulation based methods using non-uniform electric fields, like dielectrophoresis (DEP) are usually much softer than mechanical methods, offering a less destructive alternative for integrating nanostructures in electronic devices. Here, we report a feasible and reproducible dielectrophoretic method to assemble single GaAs NWs (with radius 35–50 nm, and lengths 3–5 μm) on conductive electrodes layout with assembly yields above 90% per site, and alignment yields of 95%. The electrical characteristics of the dielectrophoretic contact formed between a GaAs NW and conductive electrodes have been measured, observing Schottky barrier like contacts. Our results also show the fast fabrication of diodes with rectifying characteristics due to the formation of a low-resistance contact between the Ga catalytic droplet at the tip of the NW when using Al doped ZnO as electrode. The current-voltage characteristics of a single Ga-terminated GaAs NW measured in dark and under illumination exhibit a strong sensitivity to visible light under forward bias conditions (around two orders of magnitude), mainly produced by a change on the series resistance of the device.

Keywords: optoelectronics, nanowire assembly, dielectrophoresis, nanofabrication, chemical beam epitaxy, GaAs nanowire photodetector

(Some figures may appear in colour only in the online journal)

1. Introduction

Nowadays, there is still a growing research on inorganic nanostructures such as semiconductor nanowires (NWs) fostered by the great progress achieved during the last decades on advanced synthesis techniques, including molecular beam epitaxy (MBE) [1–5], chemical beam epitaxy (CBE) [6, 7] and chemical vapor deposition (CVD) [8–11]. The controlled growth of high-crystal quality NWs made of different materials (e.g. III–V [2, 3, 5–7], IV [9], metal oxides [10], etc) and complex architectures such as NWs based on core–shell [1, 4] or quantum wells [11, 12], has been successfully demonstrated mainly through bottom-up based growth mechanisms. Resulting NWs present unique properties such as high NW length-to-diameter ratios—namely aspect ratios—above 100, high surface-to-volume ratios, high crystal quality, and nanometric foot-prints (diameters < 100 nm), allowing them to show quantum effects [12–14], surface optical phonons [15], ultra-high photo-gains [16, 17], as well as, higher signal-to-noise ratios [18], higher sensing surface [18, 19], higher integrability [20–24], higher mechanical properties [24] and

faster switching speeds than those obtained by their counter parts the thin film and bulk materials used in conventional electronics and optoelectronics. Due to above features, semiconductor NWs have extensively probed their validity and applicability as building blocks of a wide number of applications, including optoelectronics, electronics, photonics, photovoltaics, and sensing applications [16, 25–27]. However, the compatibility of NWs with conventional nanofabrication tools is still a critical bottleneck, hindering the efficient integration of NWs in aforementioned applications, and therefore the effective deployment and commercialization of NW based technology in the market. The manipulation and transferring of NWs from the growth substrate to a foreign receiver substrate to realize those applications, is still a challenge that needs further investigations [20–24].

Assembly techniques based on mechanical forces (contact-printing, stamp-printing and roll-printing) or fluidics (Langmuir–Blodgett and bubble-blown) have demonstrated their validity to produce a large-area, compact, and uniform electronic layers based on multiple semiconducting NWs [20, 22–24, 28]. Although some of these techniques have demonstrated certain control over the density of assembled NWs and potential to fabricate 3D stacked structures, [21, 22, 24], they lack control over single NWs, which is interesting for the investigation of their fundamental properties and mechanisms. Moreover, single NW based devices could be particularly interesting for the design of high-performance applications such as single photon detectors or single molecule chemical sensors [29]. Assembly techniques such as dielectrophoresis (DEP) [16, 30–35], optoelectronic tweezers (OETs) [36, 37], and nano-manipulation [38] have shown high precision at the nanoscale, allowing to trap, place and align single NWs at specific places along a receiver substrate. Indeed, DEP and OET are contact-less based techniques, utilizing electric fields to assemble NWs, drastically reducing the potential risk of structural damage of NWs during their manipulation.

DEP technique has been successfully used to assemble single NWs made of different materials, including ZnO [16], Si [35], InAs [32], GaN [34], as well as carbon nanotubes (CNTs) [33], between conductive electrodes. These studies demonstrated great control over the number of trapped NWs and large assembling yields, above 90% per site, which are essential characteristics for the fabrication of electronic devices (e.g. display, electronics and sensors) with a uniform and compact distribution of NWs along the device active area. The accurate control of DEP technique on the manipulation and trapping of single NWs allows the analysis of fundamental properties of these nanostructures (e.g. quantum effects, 1D carrier transport, etc), as well as the creation of complex monolithic 3D structures. Although DEP presents a great fabrication yield and excellent processing reproducibility, this technique manipulates NWs in solution, which might inhibit the accurate control over the resulting integration performance. For example, NW bundling in solution [39], parasitic particles in the NWs solution [40], electrodes degradation, solution bubbling [41], and changes on

assembled NWs properties (electrical or even structural changes) [42], might be potentially observed during conventional DEP experiments, and therefore, are considered as critical drawbacks to be overcome during the fabrication of NW based devices by DEP. In this way, the filtration and purification of NWs solution [39], the control over the NWs solution concentration, the optimization of DEP parameters to prevent any damage on both electrodes and NWs [16], or even the development of new approaches such as contact-less DEP [43], need to be further studied for the development of high-performance devices based on NWs.

In addition to NW assembly, the feasible fabrication of stable electrical contacts on semiconductor NWs is an important challenge, since the suppression of the Schottky surface barrier is often difficult either by using a heavy doping or by varying the NW chemical composition near the contact. Recent results obtained in Au-In catalysed growths of GaAs NWs show that Schottky barrier is significantly reduced at the interface between the catalytic tip and the NW, due to the reduced density of pinning states and the formation of an electric dipole layer at the catalyst/NW interface [44]. This property of NWs grown by vapor–liquid–solid (VLS) method may enable Schottky barrier height control and low-resistance electrical contacts to be formed at the electrode-NW interface without the need for annealing or contact doping.

In this work, we present the dielectrophoretic assembly of GaAs NWs grown by Ga-assisted VLS in a CBE system [6], studying the effect of parameters such as alternating current (AC) signal amplitude and frequency on the assembling performance, i.e. NW assembling yield and resulting NW alignment. Further, DEP was used to trap and align a single GaAs NW—with and without a Ga droplet atop the NW tip—between conductive electrodes, allowing the characterization of its optoelectronic properties in dark and under illumination. The behavior of the contact formed between the electrode and the NW was also studied, obtaining feasible and reproducible procedure to fabricate single GaAs NW based Schottky barrier diodes for optoelectronic applications.

2. Theory/calculation

Conventional DEP process comprises the use of an AC signal applied between two electrodes separated a gap distance shorter than the length of the NW, as thoroughly explained elsewhere [16, 30]. Briefly, a droplet of NWs in suspension is casted on top of the electrodes gap area (*see* figure 1). NWs are then attracted from the suspension towards the electrodes gap, following the gradient of the electric field, being finally aligned by the electric field created between those electrodes. The assembly process results in a NW based bridge connecting a pair of electrodes (*see* figure 1).

The DEP assembly of NWs depends on NWs size and morphology, on dielectric properties of both NWs and solvent, and on the amplitude and frequency of the applied AC signal. Conventionally, the DEP assembly of particles has been described by either Maxwell stress tensor or effective dipole moment expressions [45]. The former is a more exact
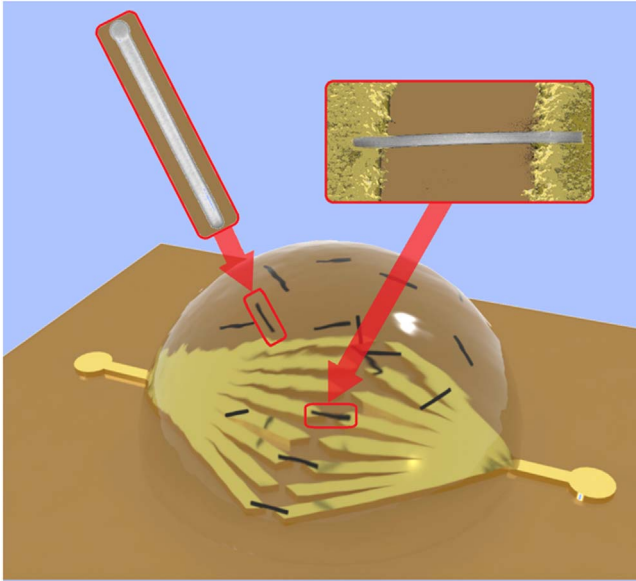
Figure 1. 3D schematic of the DEP process, during drop-casting of the NWs solution over a substrate with pre-patterned electrodes. The AC signal applied between pairs of electrodes leads to trap single NWs between the electrodes gap. Inset: scanning electron microscopy (SEM) image of a GaAs NWs in solution (left) and after DEP assembly (right).

calculation of the dielectrophoretic force (F_{DEP}) exerted on a particle in solution, and therefore, it does not involve any approximation such as spherical particle and small non-uniformity of the field gradient [46], as in the case of the effective dipole moment method. However, effective dipole moment method has been extensively demonstrated to be a valid approach for trapping particles at gaps with a smaller size than the particle size (in this case, the length of a NW is typically in the range of tens of microns) [16, 32, 33, 47].

Effective dipole moment method is the simplest way to calculate the F_{DEP} exerted on a spherical particle, being calculated as follows [33]:

$$F_{DEP} = \varepsilon_m \, c \, \Re[f_{cm}] \nabla \, |E|^2, \qquad (1)$$

where ε_m is the dielectric permittivity of the medium (i.e. solvent of the NWs solution), E is the electric field, and c is the shape-volume factor of the particle. For a cylindrical shape particle, like a NW, the parameter c depends on NW radius (r_{NW}) and length (L_{NW}) through the equation

$$c = \frac{1}{2} r_{NW}^2 \, L_{NW}. \qquad (2)$$

$\Re[f_{cm}]$ is the real part of the Classius–Mossotti factor (f_{cm}), whose generalised expression for a prolate ellipsoid (good approximation of the cylindrical shape of a NW) is given by

$$f_{cm} = \frac{\varepsilon_p^* - \varepsilon_m^*}{\varepsilon_m^* + L_i \, (\varepsilon_p^* - \varepsilon_m^*)}, \qquad (3)$$

L_i being the depolarization factor, which depends on the relative orientation of the NW respect to the electric field. ε_p^* and ε_m^* are complex dielectric permittivities of the NW and

the medium, respectively, which can be calculated as

$$\varepsilon^* = \varepsilon - j\frac{f\sigma}{2\pi}, \qquad (4)$$

where ε and σ are the dielectric permittivity and the electrical conductivity, respectively, and f is the AC frequency. From above expressions, when using AC signals, it is worth noting that F_{DEP} depends on time. Since this dependence occurs through $\nabla|E|^2$ magnitude, the F_{DEP} results in a pulsed force whose modulus (i.e. intensity of the force) changes over time, but in contrast, its direction remains unchanged. In this regard, an AC based F_{DEP} could be conveniently expressed as an average force, i.e. $\langle F_{DEP} \rangle$ whose value is proportional to the square of the root-mean square voltage (V_{rms}) of the applied AC signal. Summarizing, $\langle F_{DEP} \rangle$ depends on f through equations (1), (3), (4), on V_{rms} through $\nabla|E|^2$ in equation (1), and on the NW dimensions (i.e. r_{NW} and L_{NW}) shape, and orientation with respect to E (i.e. through the L_i factor) through equation (2). In the following sections, we will analyze the influence of above parameters on the trapping and assembly of GaAs NWs by DEP.

3. Materials and methods

3.1. GaAs nanowires synthesis and characterization

GaAs NWs were grown on oxidized Si(111) substrates in a CBE system using triethylgallium (TEGa) and tertiarybutylarsine (TBAs) as Ga and As metalorganic precursors, respectively. The growth procedure is based on Ga-assisted VLS mechanism thoroughly investigated and described elsewhere [48, 49]. Prior to the NW growth, Si(111) substrates were firstly etched in a buffered HF:H$_2$O solution (1:9 in volume) for 5 min—to remove the native oxide of the substrate—and thereafter oxidized in air at room temperature for 5 min (figure 2(a)). Resulting Si(111) presents a SiO$_x$ surface layer with a thickness of 0.5 nm—as determined by spectroscopic ellipsometry—and a random distribution of pinholes. Then, the substrate is annealed at 650 °C for 5 min under ultra-high vacuum conditions in the CBE chamber to desorb any potential contamination attached during the loading of the substrate into the CBE system (figure 2(a)). When the TEGa flux is opened, TEGa molecules in contact with the substrate are either: (1) thermally decomposed producing Ga atoms, or (2) directly desorbed from the substrate surface and pumped out the system (figure 2(b)). In this scenario, Ga atoms tend to form nanodroplets preferentially at SiO$_x$ pinholes as demonstrated by scanning electron microscopy (SEM) (figures 2(b1)–(b3)), and whose size mainly depends on factors such as TEGa flow, TEGa pre-deposition time and stabilization time after the TEGa pre-deposition as demonstrated elsewhere [48, 49]. Thereafter a stabilisation step—where TEGa is switched off for 1 min, allowing the rearrangement of Ga droplets and stabilization of the resulting Ga droplet size—both TEGa and TBAs flux are opened, leading to the formation of (Ga,As) alloy at each droplet (figure 2(c)). This alloy tends to supersaturate, resulting in the precipitation of GaAs towards the interface formed
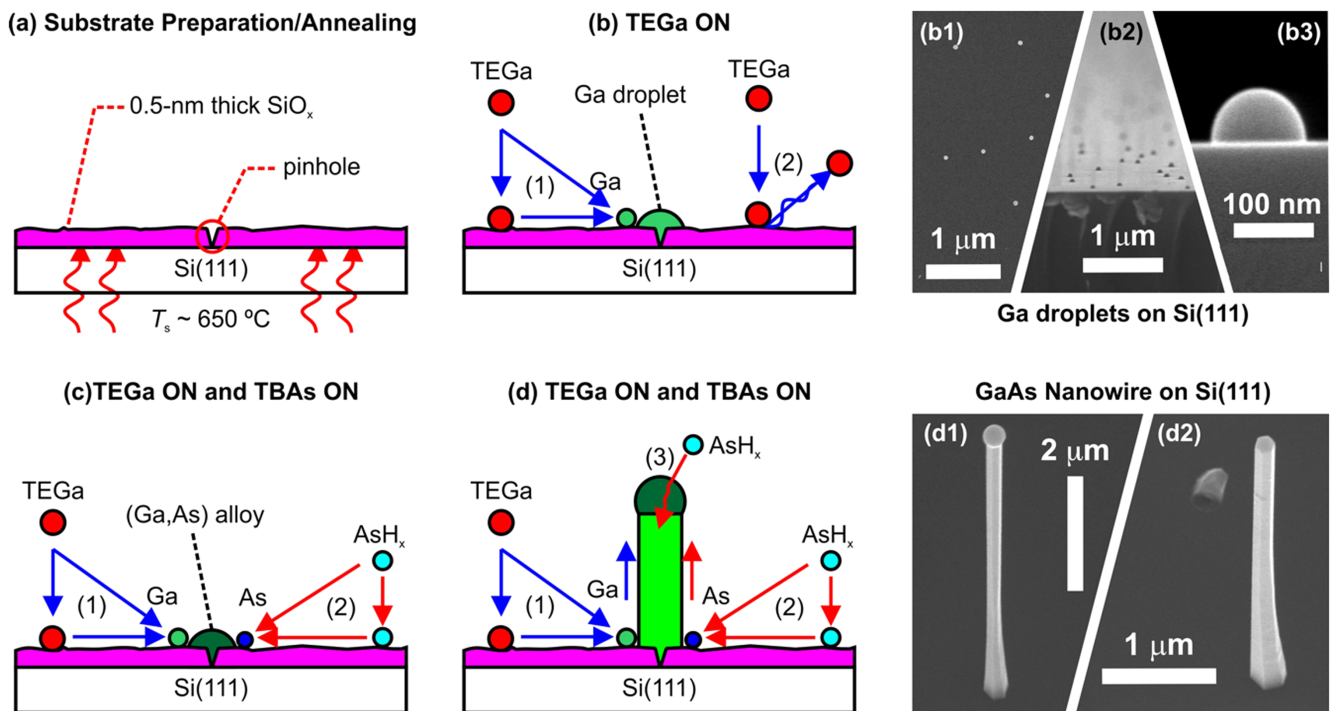
Figure 2. (a)–(d) Picture of Ga-assisted VLS growth of GaAs NWs on Si(111) substrates by CBE, comprising: (a) native oxide etching in HF buffered solution, and subsequent oxidation in air ambient, and a thermal annealing at a substrate temperature $(T_s) = 650\ °C$ in high vacuum conditions for 5 min, resulting in 0.5 nm thick oxide layer with nano-pinholes; (b) Ga droplet pre-deposition (SEM images: (b1) top-view, (b2) 30° tilted view, and (b3) cross-section view); (c) formation of (Ga,As) liquid alloy until As saturation is reached; (d) GaAs NW growth under the Ga droplet (SEM images: GaAs NWs (d1) with and (d2) without Ga droplet atop the NW tip).

between the droplet and the Si(111) substrate surface. The growth of the GaAs NWs is observed under each Ga droplet (figure 2(d)). The morphological characterization of the resulting sample shows GaAs NWs vertically aligned on the surface of the Si(111) substrate (figure 2(d1)), with a hexagonal and nanometric footprint, typical radius ranging between 30 and 50 nm, growth rates around $4–5\ \mu m\,h^{-1}$, pure zinc blende structure [49], and NWs densities ranging between $0.4\ NWs\ \mu m^{-2}$. The NWs density observed by SEM roughly corresponds to the initial density of Ga droplets obtained after the TEGa pre-deposition and subsequent stabilisation (figure 2(b1)). From figures 2(d1), (d2) one can observe variations in the resulting NW diameter and a non-uniformity of the NW diameter along the stem, also known as tapering. The difference observed on the diameters of the NWs and tapering effect shown in figures 2(d1), (d2) are mainly caused by the initial size of the Ga catalyst (figures 2(b1)–(b3)) and the growth conditions (Ga/As flux ratio, total gas flow, substrate temperature, etc). The method described in figures 2(a)–(d), used to pre-deposit Ga droplets along the substrate surface, results in a broad distribution of droplet diameters, causing different initial conditions for each NW. Once the growth starts, i.e. both TEGa and TBAs fluxes are opened, the surface underneath the droplet defines the size of the NW root. However, depending on the Ga/As flux ratio, the size of the Ga droplet—and also the NW cross section—could be re-adjusted until reaching a constant size, when a uniform NW diameter is provided (i.e. steady-state conditions at the growth interface).

3.2. GaAs nanowires suspension

The suspension containing GaAs NWs with Ga droplets on their tips (figure 2(d1)) namely suspension A, was prepared by dipping an as-grown NWs sample ($0.4\ NWs/\mu m^2$) with a dimension of 1 cm² in 1.5 ml of ethanol, and sonicating it for a few seconds. NWs are detached from the growth substrate and released to the solvent. The SEM characterization of the growth substrate right after the sonication step exhibits that approximately 100% of the initial NWs were successfully detached from the substrate and thus released to the solvent, resulting in a concentration of around $3 \times 10^8\ NWs/ml$.

On the other hand, the suspension containing GaAs NWs without Ga droplets (figure 2(d2)), namely suspension B, was prepared by firstly etching a 1 cm² NW sample (with a NW density of around $0.4\ NWs/\mu m^2$) in a buffered solution of $HCl:H_2O$ (1:9) for 1 min, in order to etch completely Ga droplets, exhibiting then a flat NW front (figure 2(d2)). After the Ga droplet etching, NWs were removed from the substrate and transferred to the solvent following the same procedure described above for the suspension A.

3.3. DEP system description

The DEP system utilized in this work consists in a probe station adapted to allow deposition of droplets extracted from the NW solutions on the receiver substrate surface, under a clean and controlled environment. The probe station was sealed, preserving the NWs solution to get contaminated and

minimizing the uncontrolled evaporation of the droplet solvent during DEP experiments. The temperature and humidity were measured prior to each experiment by using a digital hygrometer in order to confirm the feasibility of the experimental results.

The theoretical estimation of the expected number of assembled NWs as a function of the DEP conditions was confirmed by experimental results obtained using long and wide Al electrodes (100 μm long and 100 nm thick) with a gap of 2 μm, enabling the assembly of multiple NWs in single DEP runs. The fabrication of Al electrodes was carried out by using DC magnetron sputtering and photolithography on SiO$_2$(300 nm)/Si substrates. The fabrication of the photodetectors was developed using AZO electrodes, whose work function is compatible with GaAs, benefiting the formation of a good electric contact after the DEP assembly. 100 nm thick AZO electrodes were defined on top of SiO$_2$(300 nm)/Si substrates by RF magnetron sputtering and photolithography. The shape of the electrodes (i.e. the width of the tip around tens of microns) was chosen in order to allow the assembly of single NWs.

The DEP system has three main parts: (i) waveform function generator (HAMEG-HMF2550); (ii) semiconductor parameter analyzer (HP4145B); (iii) LED based light source. The role of the waveform function generator is to supply an AC sinusoidal signal to the pair of electrodes to create the DEP force. The generator operates at a frequency range ranging from 10 kHz to 1 MHz with a V_{rms} ranging from 0.5 to 7 V. The semiconductor analyzer permits to measure the *I–V* curve of the assembled NWs during the DEP experiments. A red LED was mounted on a holder right above the sample surface, enabling to measure the response of trapped NWs to the irradiation of light. This all-in-one system allows a quick analysis of the DEP assembling yield.

The DEP experiments are developed in three steps. Firstly, as the function generator is switched on, a drop of NWs suspension (5 μl) is applied onto the sample surface. This volume was chosen because it enables to cover the whole trapping area. After 2 min holding the AC signal ON, the sample surface is rinsed with DI water, ethanol, and dried in a stream of N$_2$ gas. Right after, the function generator is switched off.

3.4. Photoresponse characterization

The visible light source used in this work was a Halogen Light Source (from Ocean Optics, DH-2000) with a wavelength range of 300–1500 nm, and a power (P^*) of 100 W, which results in a power density of 0.13 mW cm^{-2}. The light was directed from the visible lamp through an optical fiber, and was focused on top of the GaAs NW area by an optical lens. P^* is therefore the power of the light source measured with a semiconductor power meter placed at the equivalent position of the sample. To estimate P, the NW was considered as a hexagonal prism (figure 3(a)) with a lateral area exposed to the light of $A_{\mathrm{NW}} = 3\, r_{\mathrm{NW}}\, L_{\mathrm{NW}}$ (i.e. approximately half of the prism surface). Assuming that GaAs NWs have a reflectivity (R) and a absorption coefficient (α) of 5% [50] and

2.2 $\times$ 10^7 m^{-1} [51], respectively, in the wavelength range under investigation, P is as follows:

$$P = P^* \frac{A_{\mathrm{NW}}}{A_{\mathrm{beam}}} (1 - R)\, [1 - \exp(-2\alpha r_{\mathrm{NW}})]. \qquad (5)$$

P^* being the power of the light source, and A_{beam} being the area of the circular spot (beam radius, $r_{\mathrm{beam}} = 5$ mm). This calculation results in a P of 8.07 $\times$ 10^{-5} W and is based on the highly uniform optical density, which presents peak-to-valley power fluctuations lower than 5% of the average power density throughout the beam area as calibrated elsewhere [16].

4. Results and discussion

GaAs NWs used in this work were grown on oxidized Si(111) substrates in a CBE system by the self-assisted VLS mechanism thoroughly depicted in figures 2(a)–(d) (*see* Methods section for further details) and previously described [6, 48, 49]. This method has demonstrated a great control over the resulting NW density and NW aspect-ratio through the accurate pre-deposition of Ga droplets (figures 2(b1)–(b3)).

The integration of these NWs over an electrodes layout has been carried out by the DEP procedure previously reported elsewhere [16, 52]. This assembly technique requires the previous preparation of a NWs suspension in a liquid solvent. For this purpose, two different suspensions were prepared—using ethanol as solvent—consisting in GaAs NWs with (figure 2(d1)) and without (figure 2(d2)) a Ga droplet on top of their tips, aiming to analyze the effect of the Ga droplet on the resulting NW-electrode contact quality formed after the DEP assembling process (*see* Methods section for further details). For the sake of clarity, we have named as A and B NWs suspensions with and without Ga droplet, respectively.

4.1. Characterization of GaAs nanowires in suspension

Morphological properties of both as-grown GaAs NWs and GaAs NWs in (A) and (B) suspensions were thoroughly analyzed by scanning electronic microscopy (SEM) right after substrate sonication in the solvent (*see* Methods section). Firstly, the substrate was extracted from the solution and dried in N$_2$ flow, being the resulting sample morphology analyzed by SEM (figure 3(a)). This SEM image shows six remaining GaAs crystals whose thin residual thickness demonstrates that NWs fracture—caused by sonication—occurs near the NW base, preserving the as-grown NW length almost intact after the sonication (*see* inset of figure 3(a)). In addition, it is observed that all crystals present a hexagonal foot-print and exhibit the same relative crystal orientation which is an evidence of the epitaxial growth on Si(111) [6, 48, 49]. The gray color gradient observed in figure 3(a) indicates that all NWs exhibit a fracture along a tilted preferential crystalline plane, not parallel to the Si(111) substrate surface. The fracture yield obtained under the sonication conditions used in this work allowed us to have an accurate control over the NW
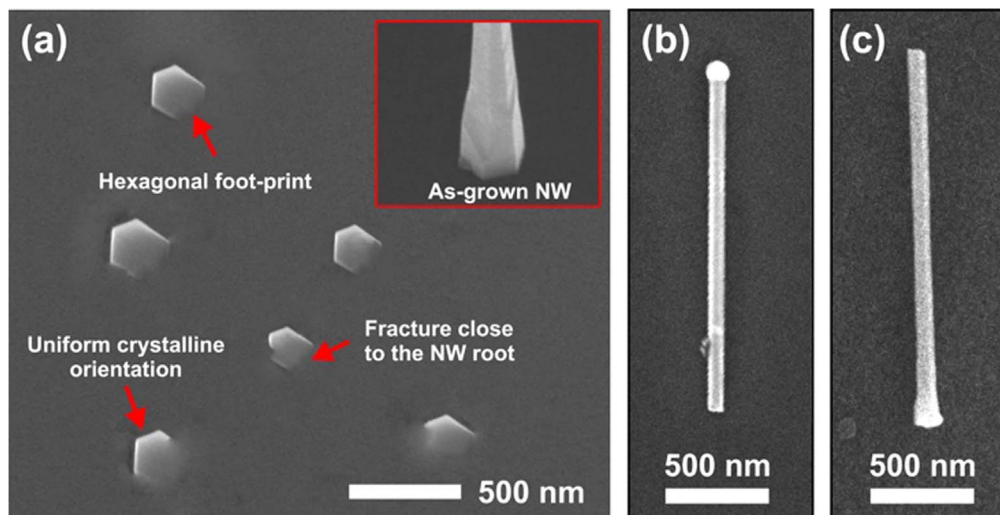
Figure 3. (a) SEM image of a substrate after the sonication step (i.e. after GaAs NWs are detached from the Si(111) surface); inset: high magnification SEM image of the as-grown NW root. SEM images of GaAs NWs (b) with and (c) without Ga droplet, after sonication and drop-casting on a Si substrate.

concentration in the resulting suspension. However, the existence of parasitic species such as nanocrystals and traces in the as-grown NWs sample [49], hinders the purity of the resulting suspension. The optimization of the NW growth approach would allow to obtain NWs suspension with better quality, as we have recently shown elsewhere [6].

A droplet extracted from each suspension (A) or (B), was drop-casted on a Si substrate, and after the solvent was completely evaporated, the morphology of GaAs NWs with (figure 3(b)) and without Ga droplet (figure 3(c)) was observed by SEM. In these images, it is noticed that: (i) both kinds of NWs preserve the length obtained during the growth; (ii) HCl:H_2O buffered solution used to etch Ga droplet from the GaAs NW tip also preserves the morphology of the NW stem; (iii) the sonication could break the NW either above (figure 3(b)) or below (figure 3(c)) the tapering region.

4.2. Performance of DEP assembly

The DEP system developed for this work allows to control the parameters of the AC signal supplied to the trapping electrodes, including the V_{rms} and f in a controlled environment (*see* Methods for further details). The DEP performance has been analyzed as a function of DEP parameters such as V_{rms} and f, using GaAs NWs without Ga droplet, i.e. NWs in solution B (figure 2(d2)). The average DEP force $\langle F_{DEP} \rangle$ exerted on a single GaAs NW has been calculated using equation (1) as a function of both, V_{rms} and f, assuming NWs with dimensions of $r_{NW} = 50$ nm and $L_{NW} = 5 \mu$m (obtained from SEM analysis), with electrical properties given by $\varepsilon_p = 10.89\varepsilon_0$ and $\sigma_p = 6000$ S m^{-1}, and suspended in an ethanol medium ($\varepsilon_m = 24.3\varepsilon_0$ and $\sigma_m = 10^{-5}$ S m^{-1}).

For frequency response studies, we have used a V_{rms} of 7 V, assuming a GaAs NW initially aligned to the electric field ($L_i = 0$) and vertically placed 10 μm away from the electrodes gap. Figure 4(a) shows the obtained results, observing a typical low-pass response with three different regions. After the initial constant force region for $f < 100$ Hz, a linear decrease of $\langle F_{DEP} \rangle$ is observed ($\langle F_{DEP} \rangle \sim 1/f^2$) when increasing the applied AC frequency. A Maxwell–Wagner dielectric dispersion such as the one characterized in the equation (1) is expected to show a low-pass response over a decade. However, it is worth noting from figure 4(a) that our dispersion of NWs exhibits a low-pass response for over five decades, indicating that the NWs dispersion analyzed in this work consists of NWs with different dielectric properties, widening the low-pass response up to 5 decades. The measurement of the low-pass response is therefore an effective procedure to determine the homogeneity of the dielectric properties of the NWs.

Finally, $\langle F_{DE} \rangle$ exhibits low constant values for $f > 30$ MHz. At a first sight, it could be deduced from this figure that the low frequency range should be better to assemble GaAs NWs due to the large force values achieved in this region, but experiments show the opposite outcome. At low frequencies ($f < 100$ Hz), the behavior of DEP is rather similar to a DC signal. In this scenario, the utilization of a DC signal in DEP at voltages in the range of 1–10 V, usually leads to the electrolysis of the suspension solvent (i.e. ethanol). We have observed by optical microscopy the formation of bubbles in the solvent at moderate voltages (1–10 V) during DEP experiments carried out at $f < 100$ Hz; the formation of these bubbles could repeal NWs away from the electrodes gap, hindering both the resulting NW alignment and trapping yield.

To study experimentally the effect of AC frequency on NWs assembly, DEP processes were carried out using f values up to 1 MHz, and the resulting SEM images are shown in figures 4(b)–(d). The successful trapping of GaAs NWs was observed only for $f > 10$ kHz, named assembly region in figure 4(a), involving $\langle F_{DEP} \rangle$ with values ranging between pN and nN. In this assembly region, NWs may reach a better alignment with the electric field lines because the NW assembly mechanism is carried out under lower $\langle F_{DEP} \rangle$
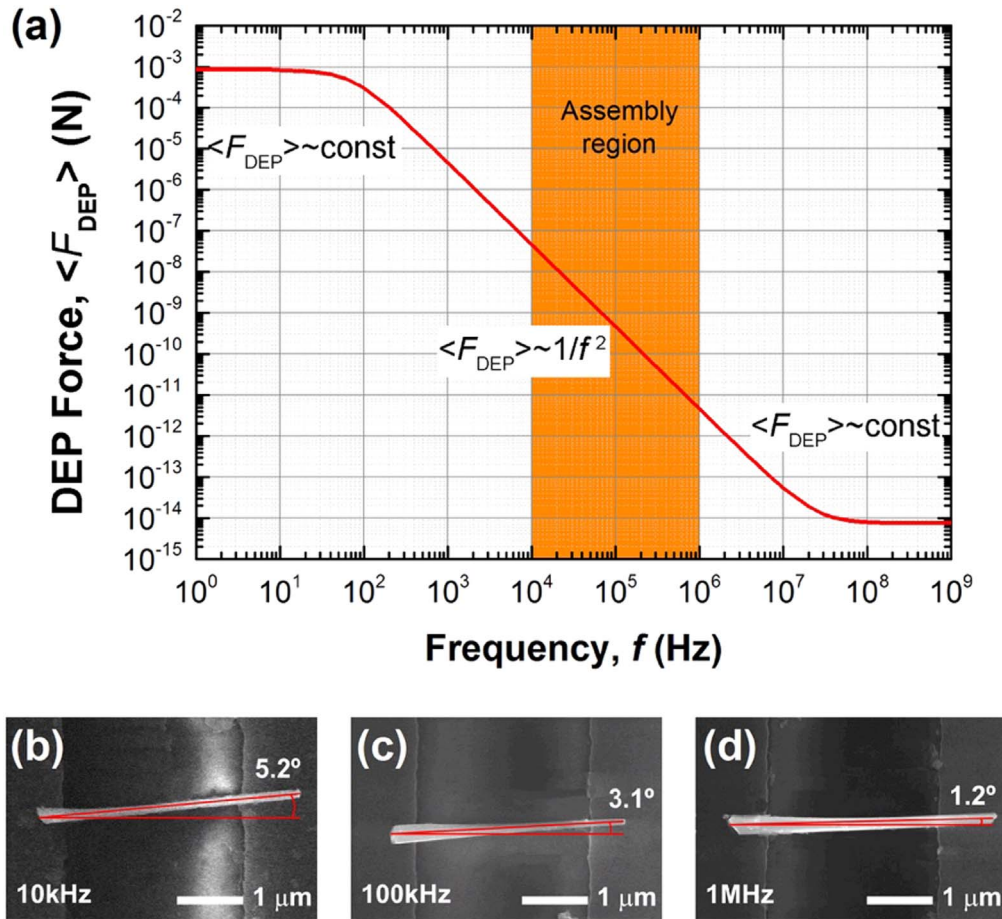
Figure 4. (a) $\langle F_{DEP} \rangle$ exerted on a GaAs NW dipped in ethanol, as a function of AC frequency (f). (b)–(d) SEM images of single GaAs NWs aligned by DEP carried out at different f values ($V_{rms} = 7$ V).

values, resulting in a slower and softer process than for low frequency values.

The effect of a softer NW alignment mechanism was analyzed in three DEP samples carried out at different frequencies within the assembly region (10 kHz, 100 kHz and 1 MHz), as shown in figures 4(b)–(d). The assembly angle—defined as the final angle between NWs and the electric field lines normal to both electrodes—is progressively reduced as the DEP frequency is increased, demonstrating the improvement of the NW alignment when increasing f from 10 kHz to 1 MHz. Under these frequency conditions, we observed an alignment yield above 95% (*see* appendix A), comprising NW misalignments below 5° with respect to the alignment direction (i.e. electric field direction). Additionally, various experiments were carried out at frequencies below 10 kHz, comprising 100 Hz, 500 Hz, 1 kHz, 2 kHz, and 5 kHz. The results obtained from these DEP experiments showed no assembly of NWs, indicating that the high value of the $\langle F_{DEP} \rangle$ demonstrated in figure 4(a) for low frequencies is not sufficient to guarantee the effective assembly of NWs. The requirement of a non-uniform electric field produced by a high AC signal is therefore essential not only to trap, but also to align NWs bridging the trapping gap between electrodes, creating functional devices. In this regard, both AC frequency and applied voltage need to be investigated and optimised in

order to compensate the poor performance of the DEP assembling rate observed at low frequencies.

It was previously mentioned, the $\langle F_{DEP} \rangle$ exerted on a GaAs NW depends on the applied AC voltage through the $\nabla|\boldsymbol{E}|^2$ magnitude, as given by equation (1). In this way, figure 5(a) shows the calculated $\langle F_{DEP} \rangle$ values as a function of the V_{rms} value, assuming a GaAs NW initially aligned along the electric field ($L_i = 0$) and vertically placed 10 μm away from the electrodes gap, using an AC frequency of $f = 100$ kHz. The $\langle F_{DEP} \rangle$ dependence on V_{rms}, as expected from equation (1), is clearly seen in this figure, reaching values close to 0.5 nN for $V_{rms} = 7$ V. In order to check the validity of above calculations, DEP experiments were also carried out using wide-sized electrodes (100 μm) separated by a 2 μm gap, allowing the assembly of multiple NWs interconnecting both electrodes (*see* the schema in figure 5(b)). The assembly performance was studied as a function of V_{rms} by SEM after DEP (SEM images are also shown in figure 5(b)). It is noticeable that a V_{rms} value of 4.24 V is not enough to trap any GaAs NW along the full electrodes length, as confirmed from several experiments repeated under the same conditions. $\langle F_{DEP} \rangle$ value for V_{rms} of 4.24 V, is around 0.15 nN, which is not sufficiently high to overcome the drag force in the fluid. In contrast, for larger V_{rms} values, such as 5.66 and 7.07 V, $\langle F_{DEP} \rangle$ is large enough to compensate or
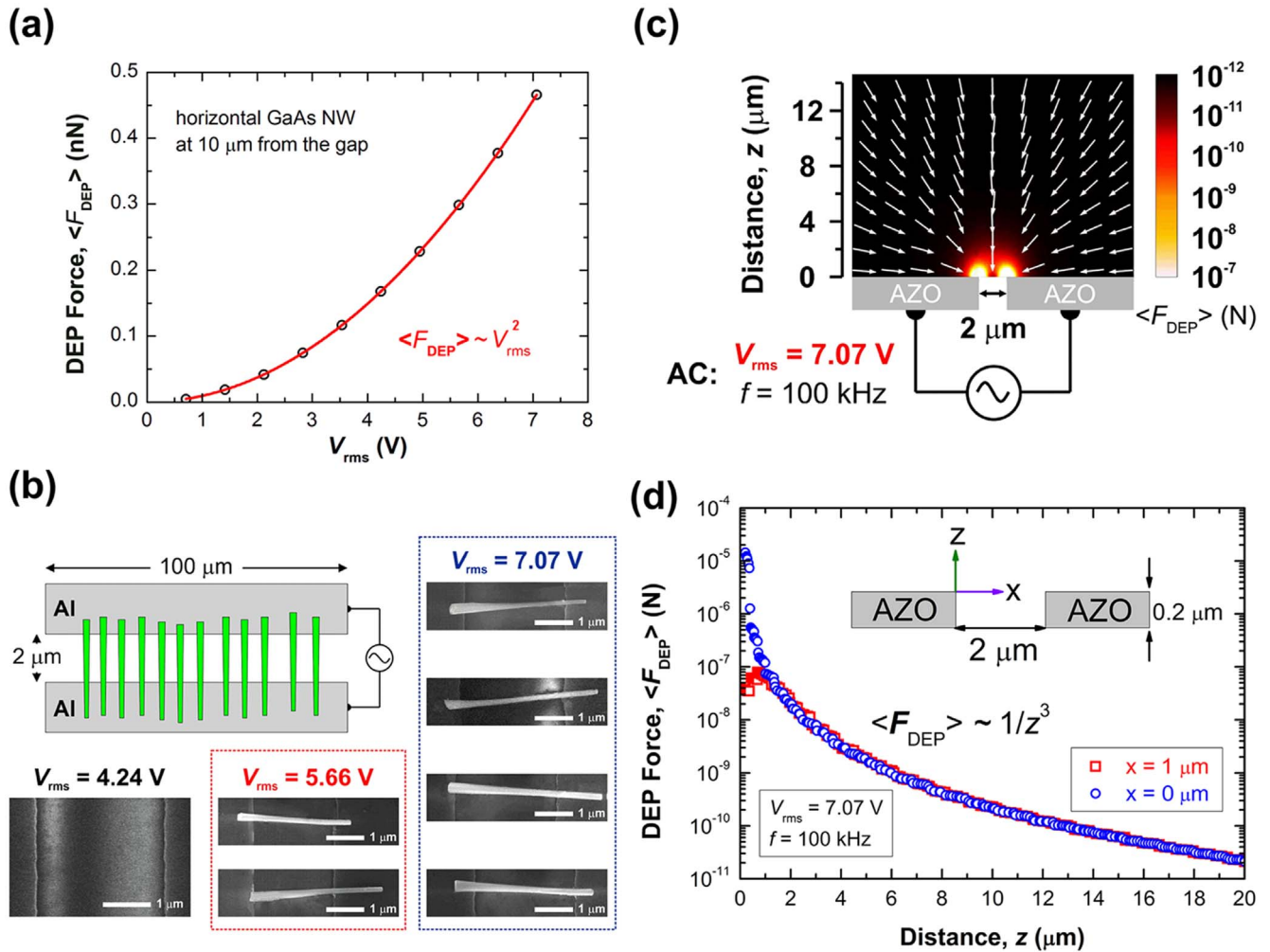
Figure 5. (a) $\langle F_{DEP} \rangle$ exerted on a GaAs NW as a function of V_{rms}. (b) SEM images of DEP experiments carried out at different V_{rms} values and schema of the electrode geometry. (c) Calculation of $\langle F_{DEP} \rangle$ as a function of the distance z, where constant magnitude arrows are used to represent $\langle F_{DEP} \rangle$ direction. (d) $\langle F_{DEP} \rangle$ amplitude versus distance z calculated at positions $x = 0$ and $1\,\mu$m; inset: schema showing the electrodes and gap dimensions, and the selected system of coordinates.

even to overcome the drag force in the fluid, resulting in the successful trapping of NWs between the electrodes gap. SEM images presented in figure 5(b) show the different NWs assembled between electrodes for the different V_{rms} values used during typical DEP experiments. For V_{rms} values of 5.66 V and 7.07 V, resulting NW densities were 0.02 and 0.08 NW μm^{-1}, respectively; the observed increase on the assembled NW density with V_{rms} is in good agreement to the trend predicted in figure 5(a).

The $\langle F_{DEP} \rangle$ exerted on a GaAs NW has been also calculated as a function of the distance between the NW and the electrodes gap, and the relative position with respect to the gap center, defined here as z and x, respectively (figure 5(c)). These calculations have been performed using $f = 100$ kHz and $V_{rms} = 7.07$ V—which are those DEP parameters exhibiting the best assembly performance—assuming a NW initially aligned along the electric field ($L_i = 0$) and an electrode spacing of 2 μm. Figure 5(c) represents a map with the directions of the calculated $\langle F_{DEP} \rangle$ by using arrows whose module is not representing the magnitude $\langle F_{DEP} \rangle$, but instead it includes a logarithmic background color scale to represent

the $\langle F_{DEP} \rangle$ magnitude. As seen in that figure, both F_{DEP} direction and magnitude are very sensitive to z, the latter taking very intense values at regions close to the inter-electrode gap. Furthermore, $\langle F_{DEP} \rangle$ arrows are clearly always pointing towards the electrode gap region, which confirms that DEP trapping mechanism occurs along the direction given by the gradient of the electric field. This is the characteristic behavior that allows for NWs trapping (positive DEP). It is worth noting again that given the dependence of $\langle F_{DEP} \rangle$ with $\nabla |E|^2$ (equation (1)), the direction of the DEP force under AC conditions does not change when the voltage is reversed every semi-period of the applied signal.

The dependence of $\langle F_{DEP} \rangle$ exerted on a single NW suspended in the solution as a function of the distance z to the electrode surface is also plotted in figure 5(d) for two different horizontal positions, i.e. $x = 0\,\mu$m (corner of one electrode) and $x = 1\,\mu$m (center of the electrode gap), as shown in the schema of figure 5(d). A fast decrease of $\langle F_{DEP} \rangle$ for large z values can be observed in that plot for both x values, whose dependence on z follows an inverse power law (z^{-3}) in that region. It is also observed in this figure for small x values that

edge of the electrodes ($x = 0\,\mu$m) attracts NWs with a stronger intensity than the position at the center of the gap ($x = 1\,\mu$m). This behavior explains the experimental observations evidencing a preferential assembly of NWs at the electrodes edge when NWs length is shorter than the gap distance. This mechanism might also benefit the soft assembly of NWs with size larger than the electrodes gap, accommodating both NW ends at both electrodes, therefore improving the reproducibility of the process.

It has been reported that the effective dielectrophoretic trapping of other semiconductor nanostructures over tens of microns requires a significant value for $\langle F_{\mathrm{DEP}} \rangle$, estimating $\nabla |\boldsymbol{E}|^2$ magnitudes in the range of $10^{-5}\,\mathrm{V}^2\,\mu\mathrm{m}^{-3}$ or even larger [53]. Our calculations result in $\langle F_{\mathrm{DEP}} \rangle$ values in the range of pN for NWs located at distances above $20\,\mu$m far from the trapping gap (figure 5(c)). However, as observed in figure 5(c) the trapping force decreases with $1/z^3$, which indicates that NWs in the solution located at distances of a few microns from the electrodes will be subjected to forces 4–5 orders of magnitudes larger than those separated from them by some tens of microns. This evidences that although the effective attraction and trapping of NWs could successfully be observed in NWs located at far distances (i.e. $20\,\mu$m and above), those which are separated only a few microns from the trapping gap will have a much higher probability to be trapped. The trapping probability also increases a factor $1/z^3$ as z decreases.

4.3. Electrode-nanowire contact properties

The optimization of the NW assembly performance through DEP parameters (i.e. $V_{\mathrm{rms}} = 5.66\,\mathrm{V}$ and $f = 100\,\mathrm{kHz}$) allowed us to carry out the assembly of a single GaAs NW between Al doped ZnO (AZO) electrodes. The characterisation of the resulting device can be easily done in a probe station without any further processing step. We have chosen AZO for the contacts mainly due to its work function ($\Phi_{\mathrm{AZO}} = 4.3\,\mathrm{eV}$ [54]), close to the work function of GaAs ($\Phi_{\mathrm{GaAs}} = 4.7\,\mathrm{eV}$ [55]) and Ga ($\Phi_{\mathrm{Ga}} = 4.2\,\mathrm{eV}$ [55]). Al electrodes have also been tested, but due to the surface oxide on top of the Al layer, the electric contact is poor, hindering the reproducibility of the measurements.

The morphological characterization of the resulting DEP assembly using NWs suspension A, i.e. Ga-terminated NWs (figure 6(a)), exhibits a clear different between AZO electrode regions contacted by the Ga droplet (figure 6(a1)) and the NW (figure 6(a2)). From figure 6(a1), one can conclude that Ga droplet was alloyed with the AZO electrode after the NW trapping. This may be a consequence of the low melting point of Ga ($\sim 30\,^{\circ}$C) and the heat generation resulting from the application of the AC signal between coplanar electrodes in a liquid medium, leading to a local increase of the temperature even for solvents with moderate ionic strengths [53]. Further, figures 6(a1) and (a2) confirm a similar contact area at both sides of the NW atop the AZO electrodes surface.

The NW configuration presented in figure 6(a) could be schematically represented as shown in figure 6(b). The *I–V* characteristics of the Ga-terminated GaAs NW clearly exhibits a rectifying behavior, as demonstrates figure 6(c) (*see also I–V* curve represented in logarithmic scale in the inset of figure 6(c)). Considering the equivalent circuit schematically presented in figure 6(b), and the general equation of the electric current through a diode [56], experimental data was fitted to

$$V = I\,R_{\mathrm{Tot}} + \mathrm{n}\,V_T \ln(I/I_{\mathrm{sat}} + 1). \tag{6}$$

R_{Tot} being the series combination of R_1 (the contact resistance between AZO electrode and Ga-droplet), R_2 (the contact resistance between Ga-droplet and GaAs NW), and R_{NW} (the intrinsic resistance of the GaAs NW) (*see* figure 6(b)); n being the ideality factor (typically around 1–2), V_T being the thermal voltage (25 mV at 300 K), I_{sat} being the saturation current, V the voltage across the diode, and I the diode current. Both R_1 and R_2 are expected to exhibit a low contact resistance, the former thanks to the similar work function of Ga and AZO, and the latter thanks to the formation of Ga-droplet/GaAs-NW contact during the VLS growth, drastically enhancing the conductivity of the resulting interface. Considering that 2D GaAs layers grown under similar conditions in our CBE system exhibit a p-type behavior due to residual carbon doping concentration around $2 \times 10^{16}\,\mathrm{cm}^{-3}$, the resistance of one of our typical NW could be estimated as $R_{\mathrm{NW}} \sim 2.5 \times 10^7\,\Omega$. This resistance should be the dominant series resistance in the equivalent circuit shown in figure 6(b), allowing to neglect both R_1 and R_2 in equation (6), resulting $R_{\mathrm{Tot}} \sim R_{\mathrm{NW}}$. The red solid lines in figure 6(c) (and also in the inset) represent the fitted curves along with the experimental data (blue circles). From that fitting, we have obtained $n = 1.00 \pm 0.08$, $R_{\mathrm{NW}} = (2.18 \pm 0.01) \times 10^7\,\Omega$, and $I_{\mathrm{sat}} = (2.5 \pm 0.3) \times 10^{-10}\,\mathrm{A}$, which should correspond to the electrical properties of the single GaAs NW measured under dark conditions. In this regard, the fitted R_{NW} value is close to the previously estimated value.

The observed *I–V* curves behave like a Schottky diode with n values close to 1 and a large series resistance, where the GaAs-NW/AZO-electrode contact should be the main responsible for the rectifying behavior; this rectifying property is an attractive feature for the development of fast response photodetectors [57, 58].

In contrast, the characterization of GaAs NWs without Ga droplet—at bias voltages ranged between -2 and 2 V—exhibits saturation currents in the pA range (orange stars in the inset of figure 6(c)). The formation of two opposite Schottky diodes consisting in GaAs-NW/AZO-electrode rectifying contacts at both sides of the NW, are considered as the main reason inhibiting the electrical conductivity through the device. Although further investigations are needed, the use of electrodes with different work functions to contact each side of the GaAs NW, would lead to diode-like characteristics which would make this kind of NW also valid for optoelectronics.

4.4. Single GaAs nanowire based photodetector

The responsivity of Ga-terminated GaAs NWs under visible illumination has been characterized to evaluate their
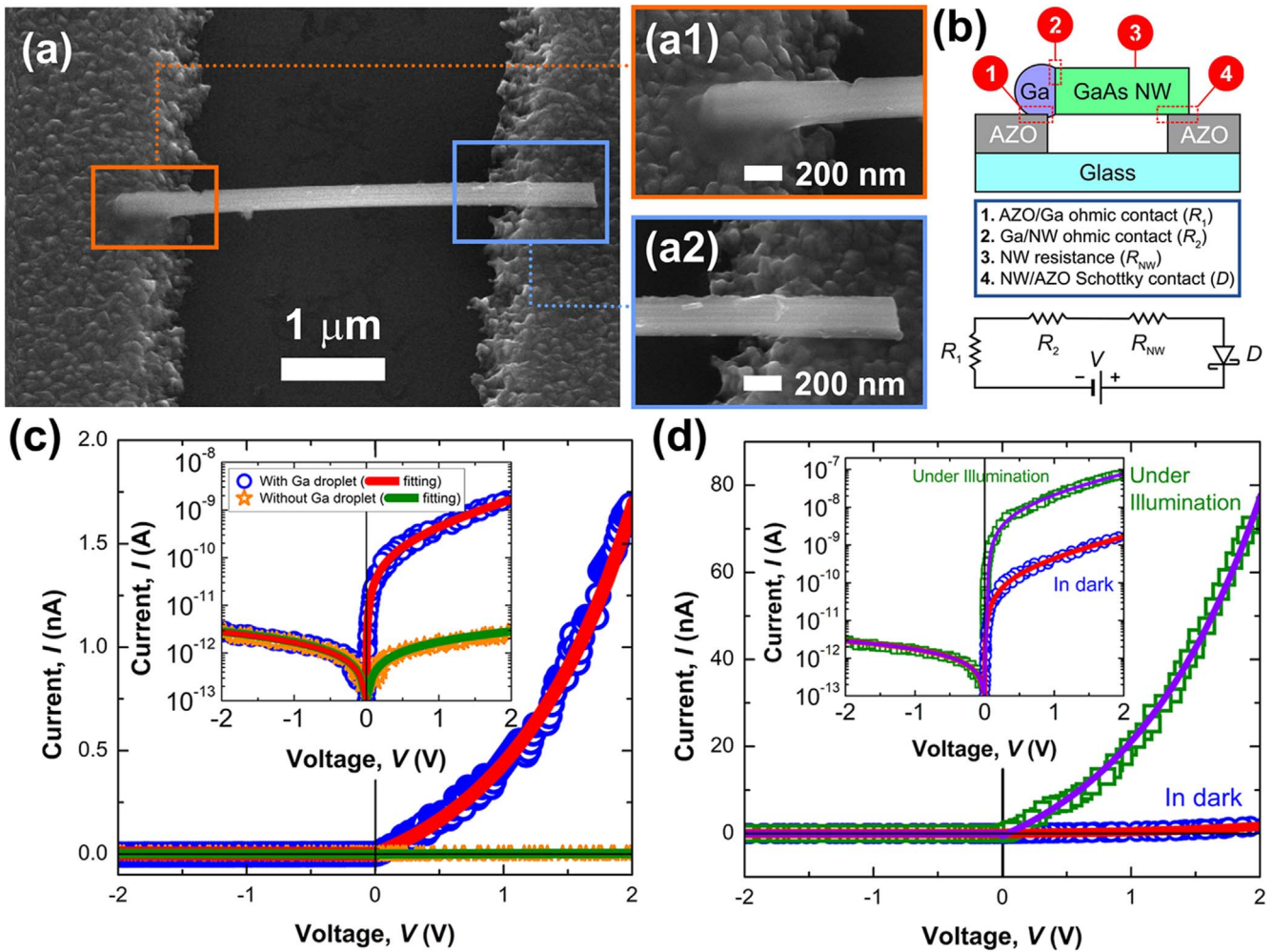
Figure 6. (a) SEM image of a Ga terminated GaAs NW assembled between a pair of AZO electrodes by DEP; high magnification SEM images of (a1) Ga droplet and (a2) GaAs NW regions in contact with the AZO electrode surface. (b) 2D schema and equivalent circuit of the hypothetic contact formed between a Ga terminated GaAs NW and AZO electrodes, assuming the existence of three resistances, including: (1) AZO/Ga ohmic contact (R_1), (2) Ga/NW ohmic contact (R_2), (3) intrinsic NW resistance (R_{NW}), and (4) NW/AZO Schottky contact (D). As detailed in the equivalent circuit, a positive bias voltage was applied to the AZO electrode in contact with the NW (i.e. negative bias voltage was applied to the AZO electrode in contact with the Ga droplet). (c) I–V characteristics of a single Ga GaAs NW with (blue circles) and without Ga droplet (orange stars) measured between AZO electrodes, and its corresponding best fitting using generalized diode equation (red and green solid lines); inset: logarithmic current versus bias voltage. (d) I–V characteristics of Ga-terminated GaAs NW measured in dark and under visible light illumination. Inset: Log(*I*) as a function of *V*.

applicability as building blocks in optoelectronic applications. GaAs NWs without Ga droplet were not included in this discussion because of their large resistance under dark conditions (*see* previous section), lacking sensitivity to visible light. For the sake of comparison, figure 6(d) shows the I–V characteristics of a Ga-terminated GaAs NW measured in dark (previously plotted with blue circles in figure 6(c)), and now also under visible light illumination. This plot exhibits an evident photosensitivity to the visible light when the device is forward biased. A clear increase of the forward current (close to 2 orders of magnitude at $V = +1$ V) can be observed in the inset of figure 6(d). The fitting of the experimental curve measured under illumination using equation (6) results in $n = 1.00 \pm 0.06$, $R_{NW} = (3.6 \pm 0.1) \times 10^4\,\Omega$, and $I_{sat} = (1.2 \pm 0.2) \times 10^{-8}$ A. The value of R_{NW} shows a reduction of around 3 orders of magnitude when compared to the value obtained under dark conditions. In addition to the

observed change in R_{NW}, the device shows some evidence of photo-generated current in the reverse bias region, where the device current is limited by the transport through the potential barrier at the contact formed by DEP between the NW and the AZO electrode.

The manipulation and assembly of single NWs by DEP facilitate the calculation of parameters such as the photo-response (R_{photo}) of the NW based photodetector, due to the dimensions of the NWs (r_{NW} and L_{NW}), and therefore, the effective area irradiated by light can be precisely estimated by

$$R_{photo} = \frac{I_{light} - I_{dark}}{P}, \tag{7}$$

where I_{dark} and I_{light} are the electrical current measured through a single GaAs NW with dimensions of $r_{NW} = 50$ nm and $L_{NW} = 5\,\mu$m (figure 6(a)) in dark and under illumination ($300 < \lambda < 1500$ nm), respectively, and P is the effective

light power absorbed by the NW (*see* Methods section). Using equation (7) and considering a applied voltage of 2 V, we obtained a R_{photo} of around 1.2 mA W^{-1} for a single GaAs NW.

The photosensitivity observed in our GaAs NWs can be explained by the change on the size of the depleted space charge region under illumination. It is well-known that GaAs surface, even covered with a native oxide, exhibits a large density of surface states located inside the bandgap, giving rise to an important band bending near the surface (Fermi level pinning) and to a carrier depleted region. When GaAs NWs are not passivated at the NW sidewalls (as it is the case for the NWs of this work), the NW body can be partly or fully depleted due to the size of the depleted region, comparable or even larger than the reduced NW diameter. This effect can reduce the effective NW section for conduction, and thus, the electrical conductance. Under illumination conditions, electron-hole pairs are created by photon absorption, increasing the carrier density in the NW body; both, band-bending and the depletion width near the NW surface are therefore reduced, leading to the increase of the NW effective section for conduction. Summarizing, the current increase observed in our GaAs NW devices is mainly attributed to a drastic reduction of R_{NW} due to the photo-generated charge carrier and the subsequent increase on the conductive volume inside the NW (figure 6(d)). In good agreement with our observations, it has been also found some similar photosensitivity mechanisms in other semiconducting NW technologies [16], where the observed reduction of the device series resistance (i.e. R_{NW}) under illumination was considered the main cause for the increase of the forward current.

5. Conclusions

In summary, GaAs NWs grown by CBE with lengths ranging between 3.5 and 5 μm have been successfully assembled between conductive electrodes separated by a 2–4 μm gap by using non-uniform electric fields via AC DEP in ethanol. Amplitude and frequency values of the applied AC signal are critical parameters to control the number of assembled NWs. V_{rms} values in the 4–7 V range, with frequencies in the 10 kHz–1 MHz range have been successfully used to align GaAs NWs with an assembly yield above 90% (see appendix A), and an alignment yield above 95% (considering only those NWs misaligned up to 5° with respect to the alignment direction). The optimization of these DEP parameters, comprising V_{rms} and AC frequency, allowed us to fabricate devices based on a single GaAs NW with and without the final Ga droplet. These results demonstrated the use of DEP as a promising, low-cost and ease of development technique for the controlled, feasible, and reproducible assembly of elongated nanostructures at specific places, allowing the fabrication of complex arrays and 2D/3D monolithic structures for multiple advanced optoelectronic applications.

I–V characteristics of single GaAs NWs with and without the final Ga droplet have also been measured. While devices

based on a GaAs NW without Ga droplet presented small currents in the pA range, both in dark and under visible illumination, devices based on Ga droplet-terminated GaAs NWs exhibited asymmetrical diode-like *I–V* curves in the pA range with an increased forward current under visible illumination. The photoresponse of 1.2 mA W^{-1} obtained at very low light power densities (0.13 mW cm^{-2}) demonstrated the viability to use single GaAs NWs based devices as photodetectors in the visible range.

For devices based on NWs without Ga droplet, obtained *I–V* curves have been explained on the basis of two opposite Schottky barrier contacts formed at both NW-electrode contacts. On the other hand, the ohmic contact between the NW end with the Ga droplet and the conductive electrode yields a rectifying behavior in devices built from Ga droplet-terminated NWs. These results prompt the use of those nanoscale ohmic contacts in the fabrication of single GaAs NW based photodetectors.

Author contributions

CGN and BJG conceptualized the work; CGN and BJG carried out the synthesis and characterization of NWs with support from AFB and NL; CGN and JLP developed the DEP system, and carried out the NWs assembly and characterization of photodetectors; CGN and BJG wrote the manuscript with support from all co-authors; BJG provided overall supervision for the project; all authors have approved the final version of the manuscript.

Conflicts of interest

The author(s) declare no competing interests.

Appendix A. Calculation of the assembly and alignment yields

The assembly yield γ_i of each experiment (i.e. single and multi-assembly of NWs) has been calculated as follows:

$$\gamma_i(\%) = \frac{n_i}{N}100,$$

where n_i is the successful number of attempts showing assembled NWs, i is the index identifying the number of

assembled NWs depending of the DEP conditions (i.e. 1, 2, 3, …) and N is the total number of attempts. For example, at DEP conditions of V_{pp} of 5.66 V and f of 100 kHz (figure 5(c)), 10 experiments were carried out, observing that 9 of them showed the same number of assembled NWs (i.e. $i = 2$), resulting in

$$\gamma_2(\%) = \frac{n_2}{N}100 = 90\%.$$

Following similar approach, the aligned yield was calculated from experiments carried out at different DEP conditions, considering NW misalignments below 5° with respect to the alignment direction (i.e. normal direction of the electrode surface).

ORCID iDs

Carlos García Núñez ⓘ https://orcid.org/0000-0001-5518-6189
Alejandro F Braña ⓘ https://orcid.org/0000-0002-2125-8495
Nair López ⓘ https://orcid.org/0000-0001-6510-1329
José L Pau ⓘ https://orcid.org/0000-0002-1371-071X
Basilio J García ⓘ https://orcid.org/0000-0002-6711-2352

References

[1] Rieger T, Grützmacher D and Lepsa M 2015 Misfit dislocation free InAs/GaSb core–shell nanowires grown by molecular beam epitaxy *Nanoscale* **7** 356–64

[2] Schuster F, Hetzl M, Weiszer S, Garrido J A, de la Mata M, Magen C, Arbiol J and Stutzmann M 2015 Position-controlled growth of GaN nanowires and nanotubes on diamond by molecular beam epitaxy *Nano Lett.* **15** 1773–9

[3] Yu X, Li L, Wang H, Xiao J, Shen C, Pan D and Zhao J 2016 Two-step fabrication of self-catalyzed Ga-based semiconductor nanowires on Si by molecular-beam epitaxy *Nanoscale* **8** 10615–21

[4] Boland J L, Conesa-Boj S, Parkinson P, Tütüncüoglu G Z, Matteini F, Rüffer D, Casadei A, Amaduzzi F, Jabeen F and Davies C L 2015 Modulation doping of GaAs/AlGaAs core–shell nanowires with effective defect passivation and high electron mobility *Nano Lett.* **15** 1336–42

[5] Matteini F, Tütüncüoglu G Z, Potts H, Jabeen F and Fontcuberta i Morral A 2015 Wetting of Ga on SiOx and its impact on gaas nanowire growth *Cryst. Growth Des.* **15** 3105–9

[6] Garcia Nuñez C, Braña de Cal A F, López N and Garcia Carretero B J 2018 A novel growth method to improve the quality of GaAs nanowires grown by ga-assisted chemical beam epitaxy *Nano Lett.* **18** 3608–15

[7] Gomes U, Ercolani D, Sibirev N, Gemmi M, Dubrovskii V, Beltram F and Sorba L 2015 Catalyst-free growth of InAs nanowires on Si (111) by CBE *Nanotechnology* **26** 415604

[8] Yang Z-X, Han N, Fang M, Lin H, Cheung H-Y, Yip S, Wang E-J, Hung T, Wong C-Y and Ho J C 2014 Surfactant-assisted chemical vapour deposition of high-performance small-diameter GaSb nanowires *Nat. Commun.* **5** 5249

[9] Moyen E, Zamfir M R, Joe J, Kim Y W and Pribat D 2016 Si nanowires grown by Al-catalyzed plasma-enhanced chemical vapor deposition: synthesis conditions, electrical properties and application to lithium battery anodes *Mater. Res. Express* **3** 015003

[10] Menzel A, Komin K, Yang Y, Güder F, Trouillet V, Werner P and Zacharias M 2015 Ultra-long zinc oxide nanowires and boron doping based on ionic liquid assisted thermal chemical vapor deposition growth *Nanoscale* **7** 92–7

[11] Ra Y-H, Navamathavan R, Yoo H-I and Lee C-R 2014 Single nanowire light-emitting diodes using uniaxial and coaxial InGaN/GaN multiple quantum wells synthesized by metalorganic chemical vapor deposition *Nano Lett.* **14** 1537–45

[12] Shi T, Jackson H E, Smith L M, Jiang N, Gao Q, Tan H H, Jagadish C, Zheng C and Etheridge J 2015 Emergence of localized states in narrow GaAs/AlGaAs nanowire quantum well tubes *Nano Lett.* **15** 1876–82

[13] Kim W, Dubrovskii V G, Vukajlovic-Plestina J, Tütüncüoglu G, Francaviglia L, Güniat L, Potts H, Friedl M, Leran J-B and Fontcuberta i Morral A 2018 Bi-stability of contact angle and its role in achieving quantum-thin self-assisted GaAs nanowires *Nano Lett.* **18** 49–57

[14] Heiss M, Fontana Y, Gustafsson A, Wüst G, Magen C, O'regan D, Luo J, Ketterer B, Conesa-Boj S and Kuhlmann A 2013 Self-assembled quantum dots in a nanowire system for quantum photonics *Nat. Mater.* **12** 439

[15] García Núñez C, Braña A F, Pau J L, Ghita D, García B J, Shen G, Wilbert D S, Kim S M and Kung P 2014 Surface optical phonons in GaAs nanowires grown by Ga-assisted chemical beam epitaxy *J. Appl. Phys.* **115** 034307

[16] García Núñez C, García Marín A, Nanterne P, Piqueras J, Kung P and Pau J L 2013 Conducting properties of nearly depleted ZnO nanowire UV sensors fabricated by dielectrophoresis *Nanotechnology* **24** 415702

[17] Wang H 2013 High gain single GaAs nanowire photodetector *Appl. Phys. Lett.* **103** 093101

[18] Rajan N K, Routenberg D A and Reed M A 2011 Optimal signal-to-noise ratio for silicon nanowire biochemical sensors *Appl. Phys. Lett.* **98** 264107

[19] Xie P, Xiong Q, Fang Y, Qing Q and Lieber C M 2012 Local electrical potential detection of DNA by nanowire–nanopore sensors *Nat. Nanotechnol.* **7** 119

[20] Yerushalmi R, Jacobson Z A, Ho J C, Fan Z and Javey A 2007 Large scale, highly ordered assembly of nanowire parallel arrays by differential roll printing *Appl. Phys. Lett.* **91** 203104

[21] Fan Z, Ho J C, Jacobson Z A, Razavi H and Javey A 2008 Large-scale, heterogeneous integration of nanowire arrays for image sensor circuitry *Proc. Natl. Acad. Sci.* **105** 11066–70

[22] Javey A, Nam S, Friedman R S, Yan H and Lieber C M 2007 Layer-by-layer assembly of nanowires for three-dimensional, multifunctional electronics *Nano Lett.* **7** 773–7

[23] Fan Z, Ho J C, Jacobson Z A, Yerushalmi R, Alley R L, Razavi H and Javey A 2008 Wafer-scale assembly of highly ordered semiconductor nanowire arrays by contact printing *Nano Lett.* **8** 20–5

[24] García Núñez C, Liu F, Navaraj W T, Christou A, Shakthivel D and Dahiya R 2018 Heterogeneous integration of contact-printed semiconductor nanowires for high performance devices on large areas *Microsyst. Nanoeng.* **4** 22

[25] Navaraj W T, García Núñez C, Shakthivel D, Vinciguerra V, Labeau F, Gregory D H and Dahiya R 2017 Nanowire FET based neural element for robotic tactile sensing skin *Frontiers Neurosci.* **11** 1–20

[26] Dasgupta N P, Sun J, Liu C, Brittman S, Andrews S C, Lim J, Gao H, Yan R and Yang P 2014 25th anniversary article: semiconductor nanowires–synthesis, characterization, and applications *Adv. Mater.* **26** 2137–84

[27] Zhang A, Zheng G and Lieber C M 2016 *Nanowires* (Berlin: Springer) pp 255–75

[28] García Núñez C, Liu F, Xu S and Dahiya R 2018 *Integration Techniques for Micro/Nanostructures Based Large-area Electronics* (Cambridge: Cambridge University Press) (https://doi.org/10.1017/9781108691574)

[29] Patolsky F and Lieber C M 2005 Nanowire nanosensors *Mater. Today* **8** 20–8

[30] García Marín A, García Núñez C, Rodríguez P, Shen G, Kim S M, Kung P, Piqueras J and Pau J L 2015 Continuous-flow system and monitoring tools for the dielectrophoretic integration of nanowires in light sensor arrays *Nanotechnology* **26** 115502

[31] Freer E M, Grachev O, Duan X, Martin S and Stumbo D P 2010 High-yield self-limiting single-nanowire assembly with dielectrophoresis *Nat. Nanotechnol.* **5** 525–30

[32] Raychaudhuri S, Dayeh S A, Wang D and Yu E T 2009 Precise semiconductor nanowire placement through dielectrophoresis *Nano Lett.* **9** 2260–6

[33] Suehiro J, Zhou G and Hara M 2003 Fabrication of a carbon nanotube-based gas sensor using dielectrophoresis and its application for ammonia detection by impedance spectroscopy *J. Phys. D: Appl. Phys.* **36** L109

[34] Kim T, Lee S, Cho N, Seong H, Choi H, Jung S and Lee S 2006 Dielectrophoretic alignment of gallium nitride nanowires (GaN NWs) for use in device applications *Nanotechnology* **17** 3394

[35] Englander O, Christensen D, Kim J, Lin L and Morris S J 2005 Electric-field assisted growth and self-assembly of intrinsic silicon nanowires *Nano Lett.* **5** 705–8

[36] Reece P J, Toe W J, Wang F, Paiman S, Gao Q, Tan H H and Jagadish C 2011 Characterization of semiconductor nanowires using optical tweezers *Nano Lett.* **11** 2375–81

[37] Zhang S, Cooper J M and Neale S L 2016 Assembling silver nanowires using optoelectronic tweezers *Advanced Fabrication Technologies for Micro/Nano Optics and Photonics IX vol 9759* (International Society for Optics and Photonics) 97590S

[38] Mølhave K, Hansen T M, Madsen D N and Bøggild P 2004 Towards pick-and-place assembly of nanostructures *J. Nanosci. Nanotechnol.* **4** 279–82

[39] Huang J, Wu Y, Gu C, Zhai M, Yu K, Yang M and Liu J 2010 Large-scale synthesis of flowerlike ZnO nanostructure by a simple chemical solution route and its gas-sensing property *Sensors Actuators* B **146** 206–12

[40] Mayousse C, Celle C, Moreau E, Mainguet J-F, Carella A and Simonato J-P 2013 Improvements in purification of silver nanowires by decantation and fabrication of flexible transparent electrodes. Application to capacitive touch sensors *Nanotechnology* **24** 215501

[41] Sanchis A, Brown A, Sancho M, Martinez G, Sebastian J, Munoz S and Miranda J 2007 Dielectric characterization of bacterial cells using dielectrophoresis *Bioelectromagnetics* **28** 393–401

[42] Saha S 2008 Nanodielectrics with giant permittivity *Bull. Mater. Sci.* **31** 473–7

[43] Shafiee H, Caldwell J L, Sano M B and Davalos R V 2009 Contactless dielectrophoresis: a new technique for cell manipulation *Biomed. Microdevices* **11** 997

[44] Suyatin D B *et al* 2014 Strong Schottky barrier reduction at Au-catalyst/GaAs-nanowire interfaces by electric dipole formation and Fermi-level unpinning *Nat. Commun.* **5** 3221

[45] Juvert J, Zhang S, Eddie I, Mitchell C J, Reed G T, Wilkinson J S, Kelly A and Neale S L 2016 Micromanipulation of InP lasers with optoelectronic tweezers for integration on a photonic platform *Opt. Express* **24** 18163–75

[46] Wang X, Wang X-B and Gascoyne P R 1997 General expressions for dielectrophoretic force and electrorotational torque derived using the Maxwell stress tensor method *J. Electrostat.* **39** 277–95

[47] Suehiro J, Nakagawa N, Hidaka S-I, Ueda M, Imasaka K, Higashihata M, Okada T and Hara M 2006 Dielectrophoretic fabrication and characterization of a ZnO nanowire-based UV photosensor *Nanotechnology* **17** 2567

[48] García Núñez C, Braña A F, López N and García B J 2015 GaAs nanowires grown by Ga-assisted chemical beam epitaxy: substrate preparation and growth kinetics *J. Cryst. Growth* **430** 108–15

[49] García Núñez C, Braña A F, Pau J L, Ghita D, García B J, Shen G, Wilbert D S, Kim S M and Kung P 2013 Pure zincblende GaAs nanowires grown by Ga-assisted chemical beam epitaxy *J. Cryst. Growth* **372** 205–12

[50] Sanatinia R, Awan K M, Naureen S, Anttu N, Ebraert E and Anand S 2012 GaAs nanopillar arrays with suppressed broadband reflectance and high optical quality for photovoltaic applications *Opt. Mater. Express* **2** 1671–9

[51] Akinlami J and Ashamu A 2013 Optical properties of GaAs *J. Semicond.* **34** 032002

[52] García Núñez C, Vilouras A, Navaraj W T, Liu F and Dahiya R 2018 ZnO nanowires-based flexible UV photodetector system for wearable dosimetry *IEEE Sensors J.* **18** 7881–8

[53] Pethig R 2010 Dielectrophoresis: status of the theory, technology, and applications *Biomicrofluidics* **4** 022811

[54] Wang W, Feng Q, Jiang K, Huang J, Zhang X, Song W and Tan R 2011 Dependence of aluminum-doped zinc oxide work function on surface cleaning method as studied by ultraviolet and x-ray photoelectron spectroscopies *Appl. Surf. Sci.* **257** 3884–7

[55] Kim J-R, Oh H, So H M, Kim J-J, Kim J, Lee C J and Lyu S C 2002 Schottky diodes based on a single GaN nanowire *Nanotechnology* **13** 701

[56] Milnes A G 2012 *Heterojunctions and Metal Semiconductor Junctions* (Amsterdam: Elsevier)

[57] Cheng G, Wu X, Liu B, Li B, Zhang X and Du Z 2011 ZnO nanowire Schottky barrier ultraviolet photodetector with high sensitivity and fast recovery speed *Appl. Phys. Lett.* **99** 203105

[58] Zhou J, Gu Y, Hu Y, Mai W, Yeh P-H, Bao G, Sood A K, Polla D L and Wang Z L 2009 Gigantic enhancement in response and reset time of ZnO UV nanosensor by utilizing Schottky contact and surface functionalization *Appl. Phys. Lett.* **94** 191103